The Astrophysical Journal, 967:77 (10pp), 2024 June 1 https://doi.org/10.3847/1538-4357/ad3cdc

Measurement of Dependence of Microlensing Planet Frequency on the Host Star Mass and Galactocentric Distance by Using a Galactic Model

Kansuke Nunota[1,2], Naoki Koshimoto[1], Daisuke Suzuki[1], Takahiro Sumi[1], David P. Bennett[3,4,5], Aparna Bhattacharya[3,4,5], Yuki Hirao[6], Sean K. Terry[3,4], and Aikaterini Vandorou[3,4,5]
[1] Department of Earth and Space Science, Graduate School of Science, Osaka University, Toyonaka, Osaka 560-0043, Japan
[2] Center for Astrophysics | Harvard & Smithsonian, 60 Garden Street, Cambridge, MA 02138, USA
[3] Code 667, NASA Goddard Space Flight Center, Greenbelt, MD 20771, USA
[4] Department of Astronomy, University of Maryland, College Park, MD 20742, USA
[5] Center for Research and Exploration in Space Science and Technology, NASA/GSFC, Greenbelt, MD 20771, USA
[6] Institute of Astronomy, Graduate School of Science, The University of Tokyo, 2-21-1 Osawa, Mitaka, Tokyo 181-0015, Japan
Received 2024 March 2; revised 2024 April 5; accepted 2024 April 8; published 2024 May 21

Abstract

We measure the dependence of planet frequency on host star mass, $M_{\rm L}$, and distance from the Galactic center, $R_{\rm L}$, using a sample of planets discovered by gravitational microlensing. We compare the two-dimensional distribution of the lens-source proper motion, $\mu_{\rm rel}$, and the Einstein radius crossing time, $t_{\rm E}$, measured for 22 planetary events from Suzuki et al. with the distribution expected from Galactic model. Assuming that the planet-hosting probability of a star is proportional to $M_{\rm L}^m R_{\rm L}^r$, we calculate the likelihood distribution of (m,r). We estimate that $r = 0.10^{+0.51}_{-0.37}$ and $m = 0.50^{+0.90}_{-0.70}$ under the assumption that the planet-hosting probability is independent of the mass ratio. We also divide the planet sample into subsamples based on their mass ratio, q, and estimate that $m = -0.08^{+0.95}_{-0.65}$ for $q < 10^{-3}$ and $1.25^{+1.07}_{-1.14}$ for $q > 10^{-3}$. Although uncertainties are still large, this result implies a possibility that, in orbits beyond the snowline, massive planets are more likely to exist around more massive stars whereas low-mass planets exist regardless of their host star mass.

Unified Astronomy Thesaurus concepts: Planet formation (1241); Exoplanets (498); the Milky Way (1054); Gravitational microlensing (672)

1. Introduction

More than 5500 planets have been discovered to date, and gravitational microlensing is one of the most effective methods to detect planets. Gravitational microlensing is a unique method that can detect planets residing in a wide range of parameter space, such as planets in the Galactic disk (Gaudi et al. 2008; Bennett et al. 2010) or bulge (Bhattacharya et al. 2021), planets around late M dwarfs (Bennett et al. 2008, S. K. Terry et al. 2024, in preparation) or G dwarfs (Beaulieu et al. 2016), and even planets around white dwarfs (Blackman et al. 2021). Measuring the planet frequency as a function of host star mass and location in our Galaxy via microlensing enables us to study the comprehensive picture of planet formation throughout our Galaxy. However, there is a difficulty in determining mass and distance in the microlensing method.

For most planetary events, the angular Einstein radius, $\theta_{\rm E}$, and Einstein radius crossing time, $t_{\rm E}$, can be measured via light-curve analysis as informative parameters of the host star. These parameters are related by the following equations:

$$t_{\rm E} = \frac{1}{\mu_{\rm rel}}\sqrt{\kappa M_{\rm L}\left(\frac{1\ {\rm au}}{D_{\rm L}} - \frac{1\ {\rm au}}{D_{\rm S}}\right)}, \quad (1)$$

$$\theta_{\rm E} = t_{\rm E} \times \mu_{\rm rel}, \quad (2)$$

where $\kappa = 8.144$ mas $M_\odot^{-1}$, $D_{\rm L}$ and $D_{\rm S}$ are the distances to the lens and source, respectively, and $M_{\rm L}$ is the lens mass. The lens–source relative proper motion $\mu_{\rm rel}$ is given by $\mu_{\rm rel} = |\boldsymbol{\mu}_{\rm L} - \boldsymbol{\mu}_{\rm S}|$, where $\boldsymbol{\mu}_{\rm L}$ is the lens proper motion vector and $\boldsymbol{\mu}_{\rm S}$ is the source proper motion vector. It is clear from these equations that the two parameters $t_{\rm E}$ and $\theta_{\rm E}$ alone cannot determine $M_{\rm L}$ and $D_{\rm L}$, even assuming that the source star is located in the Galactic bulge (i.e., $D_{\rm S} \sim 8$ kpc). Therefore, to determine the lens mass and distance, it is necessary to measure at least one of the additional quantities that determine the mass–distance relations: microlens parallax or lens brightness. However, there are too few planetary events with measured microlens parallax to obtain statistically useful constraints, since the microlens parallax signal is usually subtle and it is mostly difficult to detect such a signal with ground-based surveys. Also, the lens brightness measurements require high-angular-resolution follow-up observations several years after the event (Bhattacharya et al. 2021; Blackman et al. 2021), making it difficult to obtain sufficient statistics at this moment.

Due to these difficulties, the dependence of planetary frequency on the host star mass and the location in our Galaxy is not yet well understood. Koshimoto et al. (2021b) attempted to measure the dependence of planet frequency on both host star mass ($\sim M_{\rm L}$) and on the Galactocentric distance ($R_{\rm L}$) by assuming the planet-hosting probability $P_{\rm host} \propto M_{\rm L}^m R_{\rm L}^r$. They have compared the $\mu_{\rm rel}$ distribution for given $t_{\rm E}$ of 28 planetary events by Gould et al. (2010), Suzuki et al. (2016), and Cassan et al. (2012) with the distribution expected by a Galactic model to estimate m and r. They estimated $r = 0.2 \pm 0.4$ and concluded that there is no large dependence of planet frequency on Galactocentric distance. However, their estimate for the parameter of the dependence on host mass was highly

uncertain, $m = 0.2 \pm 1.0$. The large uncertainty in m is partly because they used the distribution of $\mu_{\rm rel}$ given $t_{\rm E}$ instead of the distribution of $t_{\rm E}$ and $\mu_{\rm rel}$. This contrivance enabled them to avoid detection efficiency calculations but corresponded to a reduction of the two-dimensional information contained in the original distribution of $t_{\rm E}$ and $\mu_{\rm rel}$ to the one-dimensional information contained in the distribution of $\mu_{\rm rel}$ given $t_{\rm E}$. This in turn means that the two-dimensional distribution of $t_{\rm E}$ and $\mu_{\rm rel}$ can be used to further constrain m and r, as long as the detection efficiency is available.

Recently, Koshimoto et al. (2023) (hereafter, K23) calculated the detection efficiency for single-lens events for the MOA-II 9 yr survey via image-level simulations. This study utilizes their image-level simulations combined with the detection efficiency for planetary signals by Suzuki et al. (2016) (hereafter, S16) to calculate the detection efficiency for planetary events of the S16 sample. By using this combined detection efficiency, we compare the ($t_{\rm E}$, $\mu_{\rm rel}$) distribution of the MOA-II planet sample (S16) with the predicted one from the Galactic model optimized toward the Galactic bulge (Koshimoto et al. 2021a) to estimate m and r.

This paper is organized as follows. We describe our method in Section 2. Section 3 presents the analysis of the S16 planetary event sample to calculate the likelihood distribution of (m, r). Discussions are presented in Section 4, and Section 5 contains our conclusions.

2. Method

We follow the method of Koshimoto et al. (2021b), except that we do not give $t_{\rm E}$ as a fixed value and instead consider detection efficiency. The main objective of this study is to estimate the dependence of planet frequency on the host star mass and the Galactocentric distance by comparing the ($t_{\rm E}$, $\mu_{\rm rel}$) distribution observed in planetary microlensing events with that distribution predicted from a Galactic model. In this paper, a Galactic model refers to a combination of stellar mass function, stellar density, and velocity distributions in our Galaxy, which enables us to calculate the microlensing event rate Γ as a function of microlensing parameters.

We denote the parameter distribution of microlensing events expected from a Galactic model as $\Gamma_{\rm all}(t_{\rm E}, \mu_{\rm rel}, M_{\rm L}, R_{\rm L})$. Note that $\Gamma_{\rm all}$ represents the parameter distribution for all microlensing events, regardless of whether each system has a planet or not, or whether each microlensing events are detected. If we assume that the planet-hosting probability is proportional to $M_{\rm L}^m R_{\rm L}^r$, the ($t_{\rm E}$, $\mu_{\rm rel}$) distribution for planetary events, $\Gamma_{\rm host}$, is given by

$$\Gamma_{\rm host}(t_{\rm E}, \mu_{\rm rel}|m, r) \propto \int dM_{\rm L} dR_{\rm L}\, \Gamma_{\rm all}(t_{\rm E}, \mu_{\rm rel}, M_{\rm L}, R_{\rm L}) M_{\rm L}^m R_{\rm L}^r. \quad (3)$$

Then, the probability of observing a planetary event with ($t_{\rm E}^{\rm (obs)}$, $\mu_{\rm rel}^{\rm (obs)}$) is given by

$$f(t_{\rm E}^{\rm (obs)}, \mu_{\rm rel}^{\rm (obs)}|m, r) = \int dt_{\rm E}' d\mu_{\rm rel}' [k(t_{\rm E}^{\rm (obs)}, \mu_{\rm rel}^{\rm (obs)}; t_{\rm E}', \mu_{\rm rel}') \times \Gamma_{\rm host}(t_{\rm E}', \mu_{\rm rel}'|m, r)\, \epsilon(t_{\rm E}', \mu_{\rm rel}')], \quad (4)$$

where $\epsilon(t_{\rm E}, \mu_{\rm rel})$ is the detection efficiency for a planetary event. Note that the dependence of detection efficiency on $\mu_{\rm rel}$ is negligible for the S16 planetary event sample as discussed in Section 3.2. $k(t_{\rm E}^{\rm (obs)}, \mu_{\rm rel}^{\rm (obs)}; t_{\rm E}', \mu_{\rm rel}')$ is a kernel function, and we adopt a Gaussian kernel,

$$k(t_{\rm E}^{\rm (obs)}, \mu_{\rm rel}^{\rm (obs)}; t_{\rm E}', \mu_{\rm rel}') = \frac{1}{\sqrt{2\pi\sigma_{t_{\rm E}}^{\rm (obs)2}}} \exp\left(-\frac{(t_{\rm E}^{\rm (obs)} - t_{\rm E}')^2}{2\sigma_{t_{\rm E}}^{\rm (obs)2}}\right) \times \frac{1}{\sqrt{2\pi\sigma_{\mu_{\rm rel}}^{\rm (obs)2}}} \exp\left(-\frac{(\mu_{\rm rel}^{\rm (obs)} - \mu_{\rm rel}')^2}{2\sigma_{\mu_{\rm rel}}^{\rm (obs)2}}\right), \quad (5)$$

where $\sigma_{t_{\rm E}}^{\rm (obs)}$ and $\sigma_{\mu_{\rm rel}}^{\rm (obs)}$ are the uncertainty of $t_{\rm E}^{\rm (obs)}$ and $\mu_{\rm rel}^{\rm (obs)}$, respectively. The introduction of a kernel function is intended to allow some uncertainty in the observed values.

Note that we use the parameter set of ($t_{\rm E}$, $\mu_{\rm rel}$) rather than ($t_{\rm E}$, $\theta_{\rm E}$) because $\mu_{\rm rel}$ is less correlated with $t_{\rm E}$ than $\theta_{\rm E}$ and usually has a smaller error bar when it is determined via the finite-source effect (Alcock et al. 1997; Yoo et al. 2004). The angular Einstein radius and the relative proper motion are represented by $\theta_{\rm E} = \theta_*/\rho$ and $\mu_{\rm rel} = \theta_*/(t_{\rm E}\,\rho)$, respectively, with the finite-source parameter ρ and the angular source radius θ_*. While $t_{\rm E}\,\rho$—which is often defined as the source radius crossing time t_*—is well determined by the light curve, as also suggested by Yee et al. (2012), ρ tends to be anticorrelated with $t_{\rm E}$. Thus, the correlation between $t_{\rm E}$ and $\mu_{\rm rel}$ is smaller than the one between $t_{\rm E}$ and $\theta_{\rm E}$. Nevertheless, we performed the same analysis by using the parameter set of ($t_{\rm E}$, $\theta_{\rm E}$) and confirmed that our results would not change significantly.

When a sample of $N_{\rm sample}$ events is given, the probability of observing those events under a specific combination of (m,r), $\mathcal{L}(m, r)$, is expressed as

$$\mathcal{L}(m, r) = \prod_{i=1}^{N_{\rm sample}} f(t_{{\rm E},i}^{\rm (obs)}, \mu_{{\rm rel},i}^{\rm (obs)}|m, r). \quad (6)$$

By calculating Equation (6) under various values of (m,r) and comparing the values of $\mathcal{L}(m, r)$, it is possible to evaluate which (m, r) values are more likely. In this paper, we calculate $\mathcal{L}(m, r)$ in a grid of 0.2 increments in the range of $-3 \leqslant m \leqslant 3$ and $-3 \leqslant r \leqslant 3$. This corresponds to applying a uniform prior distribution of -3 to 3 for m and r and calculating the posterior probability distribution.

In this study, we use the Galactic model developed by Koshimoto et al. (2021a) and their microlensing event simulation tool, `genulens`[7] (Koshimoto & Ranc 2022). This model was designed to reproduce the stellar distribution toward the Galactic bulge by fitting to the Gaia DR2 velocity data (Gaia Collaboration et al. 2018), OGLE-III red clump star count data (Nataf et al. 2013), VIRAC proper motion catalog (Smith et al. 2018; Clarke et al. 2019), BRAVA radial velocity measurements (Rich et al. 2007; Kunder et al. 2012), and OGLE-IV star count and microlensing rate data (Mróz et al. 2017, 2019). The stellar mass considered in this model ranges from $10^{-3}\,M_\odot$ to $5.3\,M_\odot$ and the typical lens mass ranges from $0.02\,M_\odot$ to $1.0\,M_\odot$. Although the model is optimized for a microlensing study toward the Galactic bulge, we would like to ensure that no significant bias is introduced in our result by the model, since our analysis strongly depends on the Galactic model used.

[7] https://github.com/nkoshimoto/genulens

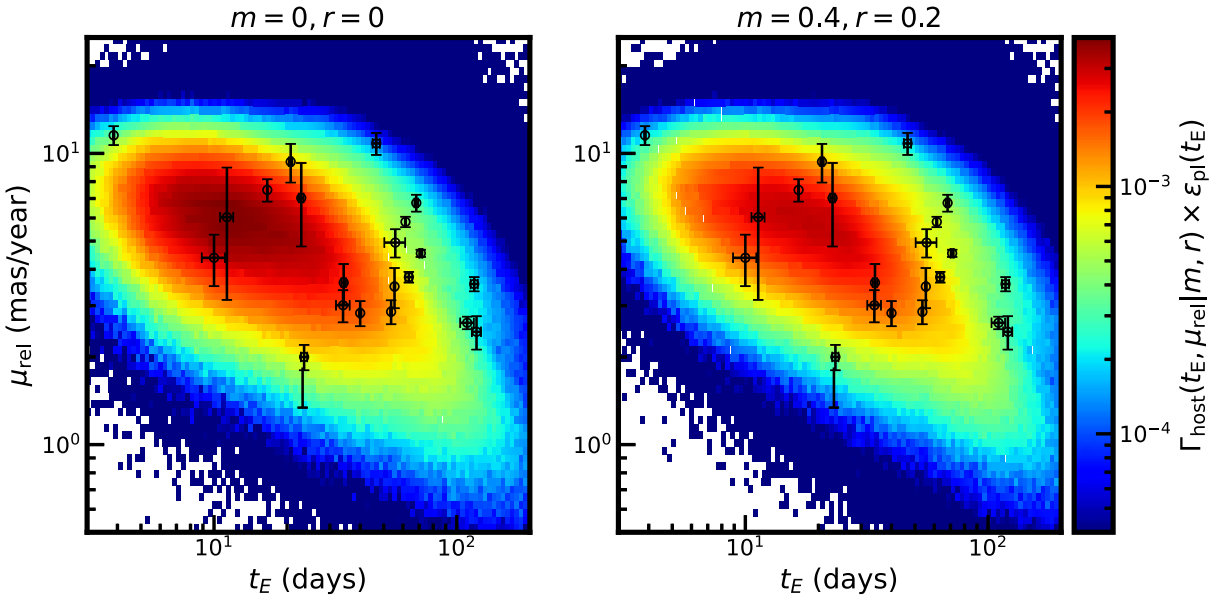

Figure 1. Comparison of the (t_E, μ_{rel}) distributions for the planetary event sample of S16 between the observations (black points) and the prediction by the Galactic model combined with the detection efficiency (color maps). The color map in the left panel shows the distribution predicted by the model with $P_{host} \propto$ const, i.e., assuming that all stars are equally likely to host planets, regardless of their mass or location in our Galaxy. The color map in the right panel is the distribution predicted by the model with $P_{host} \propto M_L^{0.4} R_L^{0.2}$, corresponding to the grid that gives the maximum likelihood.

To validate the approach of this study, we present two types of analysis in the appendices. First, Appendix A presents a mock data analysis, where we generate 50 artificial planetary events based on the Galactic model with certain (m, r) values and calculate the likelihood distributions. As a result, we confirmed this method can reproduce the input (m, r) values properly. Then, Appendix B compares the (t_E, μ_{rel}) distribution of the MOA-II 9 yr FSPL sample with the distribution predicted by the Galactic model. This confirmed no significant bias would be introduced in our result by using the Galactic model by Koshimoto et al. (2021a).

3. Application

3.1. Planetary Microlensing Event Sample

Koshimoto et al. (2021b) used 28 planetary events consisting of 22 events from the MOA-II survey during 2007–2012[8] (S16) and 6 additional events from Gould et al. (2010) and Cassan et al. (2012). The mixture of samples from different surveys was valid because they did not need to consider the detection efficiency by focusing on the one-dimensional distribution of μ_{rel} for given t_E. However, our analysis, which focuses on the two-dimensional distribution of t_E and μ_{rel}, requires consideration of detection efficiency as described in Section 2. Because the detection efficiency used in this analysis is optimized for the MOA-II survey as described in Section 3.2, we only use the 22 planetary events from the MOA-II survey as our sample in this study.

Zhu et al. (2014) predicted that 55% of planets would be detected without caustic crossing for a high-cadence microlensing survey; the KMTNet sample confirmed this prediction. On the other hand, 5 events out of our 22 planetary events were detected without caustic crossing. This indicates a higher percentage of caustic crossings than predicted by Zhu et al. (2014). This might be due to differences in observation cadence or signal-to-noise ratio between the MOA-II survey and the KMTNet survey.

The black points in Figure 1 show the (t_E, μ_{rel}) distribution of the 22 planetary events. These values are taken from the discovery or follow-up papers of each event. Some notes are as follows: MOA-2011-BLG-322 (Shvartzvald et al. 2014) has only a lower limit on μ_{rel}. MOA-2011-BLG-262 (Bennett et al. 2014) has the fast and slow solutions, but we use only the slow solution because it has a much larger prior probability as discussed in Bennett et al. (2014). The t_E and μ_{rel} values of the following events are from papers in preparation regarding follow-up high-angular-resolution imaging: MOA-2007-BLG-192 (S. K. Terry et al. 2024, in preparation), MOA-2010-BLG-328 (A. Vandorou et al. 2024, in preparation), and OGLE-2012-BLG-0563 (A. Bhattacharya et al. 2024, in preparation).

Although the following analysis will be performed with the updated values taken from the papers in preparation, we have also performed the same analysis with the values from the original discovery papers and confirmed that our results would not change significantly.

3.2. Detection Efficiency

As discussed in Section 2, our method requires the detection efficiency for the S16's planetary event sample. When calculating the detection efficiency of a sample, we need to carefully consider how the sample was collected. The event selection process of S16 can be interpreted by the following two steps: (i) the 1474 "well-monitored" events were selected from the 3300 events alerted by the MOA group during 2007–2012 based on the selection criteria summarized in Table 1 of S16, and (ii) the 22 planetary events and 1 ambiguous event were selected among them based on the χ^2 difference between the single-lens model and the planetary model. Therefore, we represent the detection efficiency for

[8] The S16 original sample consists of 23 events. However, the ambiguous event OGLE-2011-BLG-0950 turned out to be a stellar binary event (Terry et al. 2022).

Table 1
Result of the Likelihood Analysis

	All	Two-bin		Three-bin		
	$10^{-4.25} < q < 10^{-1.55}$	$q < 10^{-3}$	$10^{-3} < q$	$q < 10^{-3.5}$	$10^{-3.5} < q < 10^{-2.5}$	$10^{-2.5} < q$
$N_{\rm sample}$	22	13	9	6	10	6
m	$0.50^{+0.90}_{-0.70}$	$-0.08^{+0.95}_{-0.65}$	$1.25^{+1.07}_{-1.14}$	$0.46^{+1.29}_{-0.98}$	$-0.34^{+1.02}_{-0.57}$	$1.63^{+0.92}_{-1.18}$
r	$0.10^{+0.51}_{-0.37}$	$0.41^{+0.95}_{-0.54}$	$-0.22^{+0.68}_{-0.45}$	$0.29^{+0.98}_{-0.58}$	$0.76^{+1.22}_{-0.81}$	$-0.68^{+0.74}_{-0.78}$

Note. This table shows median and 1σ error for each sample.

the S16's planetary event sample as

$$\epsilon_{\rm pl}(t_{\rm E}) = \epsilon_{\rm WM}(t_{\rm E})\,\epsilon_{\rm ano}(t_{\rm E}), \tag{7}$$

where $\epsilon_{\rm WM}$ is the detection efficiency for the well-monitored events in S16 and $\epsilon_{\rm ano}$ is the detection efficiency for the planetary anomaly feature.

The detection efficiency for the planetary anomaly feature was calculated by S16, and we use the data shown in Figure 10 of S16 as $\epsilon_{\rm ano}(t_{\rm E})$. The dependence of the detection efficiency on $t_{\rm E}$ changes according to the mass ratio. Therefore, we use different detection efficiencies corresponding to the mass ratio for each event. In principle, the detection efficiency for a planetary anomaly feature depends not only on $t_{\rm E}$ but also on $\mu_{\rm rel}$ through the source radius crossing time, $t_* = \theta_*/\mu_{\rm rel}$, where θ_* is the angular source radius. However, as discussed in Koshimoto et al. (2021b), this effect can be considered negligible in the current case because the dependence of the detection efficiency for the anomaly feature on t_* is negligibly small for a mass ratio of $q > 10^{-4}$ (see Figure 7 of S16), which dominates our sample.

On the other hand, S16 did not calculate the detection efficiency for the well-monitored events, $\epsilon_{\rm WM}$, because they did not use the $t_{\rm E}$ information for their analysis and $\epsilon_{\rm WM}(t_{\rm E})$ was not needed. The well-monitored events were selected from the events alerted by the MOA alert system, which depends on the observer who was monitoring the light curve of each microlens candidate at the time. Although it is difficult to reproduce the exact selection process, we here utilize the results of the image-level simulation of the 6.4×10^7 artificial events conducted by K23 for their MOA-II 9 yr analysis to estimate $\epsilon_{\rm WM}$. In Figure 2, the orange dashed line and gray line show the cumulative $t_{\rm E}$ distributions for the S16 sample and 9 yr sample, respectively. We can see a lack of short-timescale events in the S16's sample compared to the 9 yr sample. This is expected because K23 studied free-floating planets, which have very short timescales, by selecting all events including short-timescale events, whereas S16 selected only well-monitored events that preferentially have longer timescales. To make the $t_{\rm E}$ distribution of the 9 yr sample closer to the S16 one, we added the S16 cut-2 criteria, i.e., $\sigma_{u_0}/u_0 < 0.40$ or $\sigma_{u_0} < 0.02$ and $\sigma_{t_{\rm E}}/t_{\rm E} < 0.25$ and $\sigma_{t_{\rm E}} < 20$ days, to the original selection process of the 9 yr sample. The blue solid line in Figure 2 shows the cumulative $t_{\rm E}$ distribution of the reselected 9 yr sample with the additional S16 cut-2 criteria, which almost perfectly follows the orange dashed line of the S16 sample. To quantify the similarity, we performed a Kolmogorov–Smirnov test on the two samples and got a p-value of $p = 0.949$, which supports the idea that the two distributions were sampled from populations with approximately the same distributions. This provides a basis for considering that the detection efficiencies of the S16 sample and the reselected 9 yr sample are almost the same. Therefore, we follow the K23 detection efficiency calculation using their artificial event sample from the image-level simulation with the S16 cut-2 criteria in addition to the original criteria listed in Table 2 of K23, and we use it as the detection efficiency for the well-monitored events, $\epsilon_{\rm WM}(t_{\rm E})$. See Appendix B.2 for an example calculation of the detection efficiency using the simulated artificial events (and see K23 for more details).

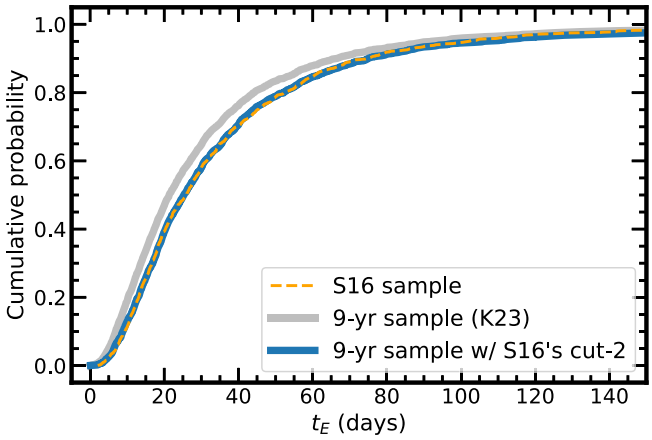

Figure 2. Comparison of the cumulative distributions of the Einstein radius crossing time, $t_{\rm E}$, among the three samples; the S16 sample (orange dashed line), the MOA-II 9 yr sample (gray solid line), and the 9 yr sample reselected by adding the S16 cut-2 criteria (blue solid line).

3.3. Likelihood Analysis

We calculate the likelihood given by Equation (6) for the 22 planetary events, and Figure 3 shows the resulted relative likelihood distribution as a function of m and r. The relative likelihood value at $(m,\ r) = (0,\ 0)$ is 0.24, and the relative likelihood takes its maximum value of 1 at $(m,\ r) = (0.4,\ 0.2)$. We find $m = 0.50^{+0.90}_{-0.70}$ and $r = 0.10^{+0.51}_{-0.37}$ from the marginalized distributions. Our result is consistent with $(m,\ r) = (0,\ 0)$, i.e., the idea that all stars are equally likely to host planets. However, it prefers $m > 0$, suggesting a possible correlation between the planet frequency and the host star mass. On the other hand, no preference is seen in either positive or negative r, which confirms the result of Koshimoto et al. (2021b), who found no large dependence of planet frequency on the Galactocentric distance.

The color maps of Figure 1 show the $(t_{\rm E},\ \mu_{\rm rel})$ distributions expected by the model, i.e., $\Gamma_{\rm host}(t_{\rm E},\ \mu_{\rm rel}|m,\ r) \times \epsilon_{\rm pl}(t_{\rm E})$, at $(m,\ r) = (0,\ 0)$ on the left and $(m,\ r) = (0.4,\ 0.2)$ on the right. Figure 1 certainly shows that the expected distribution at the best-fit grid of $(m,\ r) = (0.4,\ 0.2)$ is more matched with the observational distribution from S16 than the expected distribution at $(m,\ r) = (0,\ 0)$.

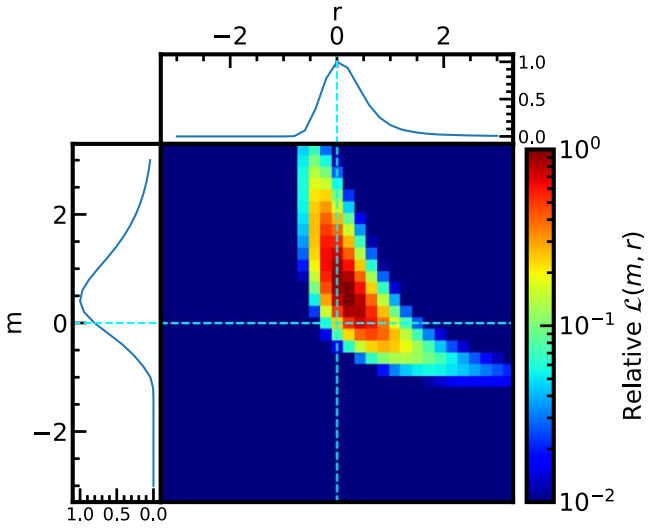

Figure 3. Relative likelihood distribution of (m, r) calculated by Equation (6) for the S16 sample of 22 planetary events. The top panel shows a relative probability distribution of r integrated uniformly over $-3 < m < 3$, and the side panel shows a relative probability distribution of m integrated uniformly over $-3 < r < 3$.

We also divide the 22-event sample into subsamples by mass ratio and perform the same analysis for these subsamples to see if there is any relationship between the mass ratio of a planetary system and planet frequency. We try two types of bin patterns for dividing the sample; the first one is the two-bin subsamples with $\log q < -3.0$ (13 events) and $-3.0 < \log q$ (nine events), and the second one is the three-bin subsamples with $\log q < -3.5$ (six events), $-3.5 < \log q < -2.5$ (10 events), and $-2.5 < \log q$ (six events).

Figure 4 shows the results of the likelihood analysis for the subsamples, where Figure 4(a) is for the two-bin subsamples and Figure 4(b) is for the three-bin subsamples. In each of Figures 4(a) and (b), the middle panel plots the mean of $\log q$ versus the median and 1σ range of the marginalized m distribution of each subsample, while the bottom panel shows those for the marginalized r values. Both results show that m is likely to be higher than 0 at the highest $\log q$ bin while m is fully consistent with 0 at the other bins. This result might suggest that massive planets are more likely to exist around more massive stars whereas low-mass planets are more universal regardless of their host star mass. On the other hand, the r value seems to have a smaller mass ratio dependence than the m value, although there is an anticorrelation between m and r.

While these are potentially interesting features, their statistics are too weak for us to conclude whether these features are real or not. We further discuss the possible dependence of m on the mass ratio in Section 4.1. The median and 1σ values of all likelihood analyses are listed in Table 1.

4. Discussion

4.1. Dependence of Planet Frequency on the Host Star Mass

We estimated the planet-hosting probability as $P_{\rm host} \propto M_{\rm L}^{0.50^{+0.90}_{-0.70}} \times R_{\rm L}^{0.10^{+0.51}_{-0.37}}$ by using the 22 planetary event sample (Figure 3 and Table 1) for planets beyond the snowline. Although all the host star masses in our sample have not been measured, the typical mass of the host star is $\sim 0.6\,M_\odot$ (S16). The result that the likelihood distribution prefers $m > 0$ suggests that the planet frequency has a possible positive correlation with the host star mass. A possible positive correlation is also seen in massive planet subsamples with $q \gtrsim 10^{-3}$, whereas m is consistent with 0 in lower-mass ratio subsamples. This implies that giant planets are more likely to exist around more massive stars, whereas lower-mass planets exist more uniformly regardless of the host star mass.

A positive correlation between planet frequency and host star mass, $M_{\rm host}$, for giant planets is also suggested by RV studies for inner planets (Johnson et al. 2007, 2010; Reffert et al. 2015). Johnson et al. (2010) analyzed 1266 stars and estimated that planet frequency is $\propto M_{\rm host}^{1.0\pm0.3}$. Their sample ranges from low-mass M dwarfs with $0.2\,M_\odot$ to intermediate-mass subgiants with $1.9\,M_\odot$. By analyzing samples from Lick Observatory, Reffert et al. (2015) found that the giant planet frequency increases with the host star mass from $1\,M_\odot$ to $1.9\,M_\odot$. Fulton et al. (2021) also suggest an increase in giant planet frequency beyond roughly $1M_\odot$ using the 178 planets discovered by the California Legacy Survey (Rosenthal et al. 2021). Importantly, part of their planet sample overlaps with our giant planet sample in the parameter space of mass ratio and semimajor axis. On the other hand, the planet samples in the RV studies do not include lower-mass planets beyond the snowline, whereas our sample does. Note that the RV planet samples were selected based on the planet masses, while our subsamples were divided based on the mass ratios.

Simulations based on the core accretion theory also suggest that the population of massive planets increases as the host star mass grows (Burn et al. 2021). In particular, at $M_{\rm host} \geqslant 0.5M_\odot$, giant planets are predicted to emerge and lead to the ejection of low-mass planets. Liu et al. (2019) and Liu et al. (2020) calculate the population of single planets around stars with masses between $0.1\,M_\odot$ and $1\,M_\odot$, and show that gas giant planets are more likely to exist around a massive star. Ida & Lin (2005) also predict that the Jupiter-mass planet frequency has peaks around G dwarfs. These theoretical results suggest $m > 0$ for massive planets, which is consistent with our result.

On the other hand, results from the Kepler telescope suggest that the frequency of sub-Neptunes at orbital periods less than 50 days is higher for M dwarfs rather than for FGK stars (Mulders 2018). These results prefer $m < 0$ for low-mass planets in inner orbits. This can be compared with our results for planets beyond the snowline that have $m = -0.08^{+0.95}_{-0.65}$ for the $q < 10^{-3}$ subsample and $m = 0.46^{+1.29}_{-0.98}$ for the $q < 10^{-3.5}$ subsample. However, the uncertainties of our results in m are large, and further investigation is needed.

4.2. Prior for Planetary Event Analysis

The results of this study are also important for the analysis of planetary events. In microlensing event analysis, Bayesian analysis using the Galactic model as a prior has been used to obtain a posterior probability distribution of the lens mass and distance. For planetary events, we have been making assumptions regarding the dependence of planet frequency on the host star mass and location in our Galaxy, i.e., assumptions on m and r in the context of this study. A traditional assumption is $(m, r) = (0, 0)$, and it has been implicitly or explicitly assumed in many studies to date (e.g., Bennett et al. 2014; Shvartzvald et al. 2014; Shin et al. 2023). Some studies consider other possibilities for m like $m = 1$ (Koshimoto et al. 2017; Ishitani Silva et al. 2022; Olmschenk et al. 2023) based on results by other techniques like RV (Johnson et al. 2010), which has a

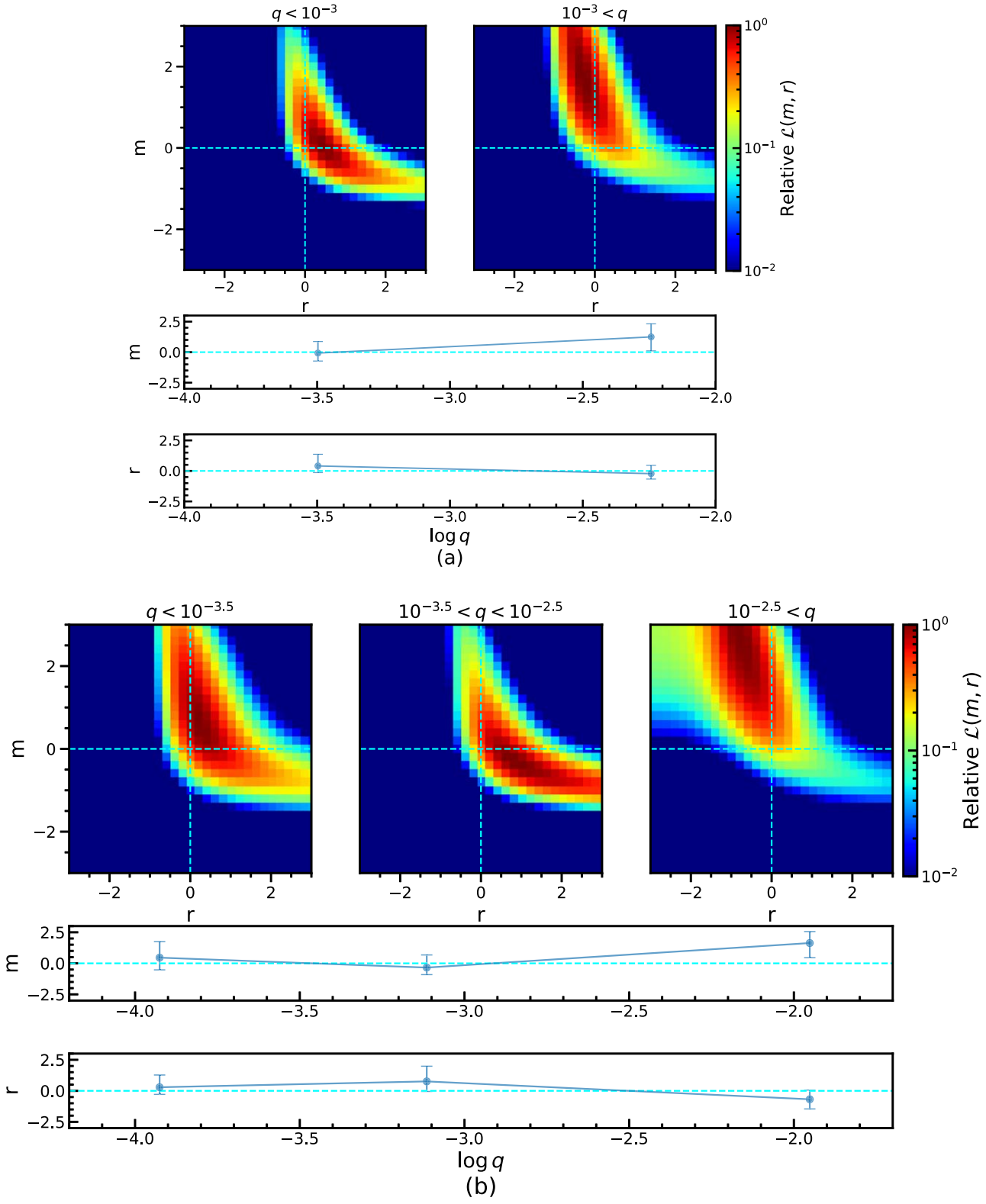

Figure 4. Relative likelihood distributions for (a) the two-bin subsamples and (b) the three-bin subsamples. In each of (a) and (b), the top panels show the likelihood distribution of (m, r) for the subsample in each bin. The middle panel shows the median and 1σ error of the marginalized m distribution vs. the mean of $\log q$ for each bin. The bottom panels are the same for the marginalized r distribution.

very different sensitivity region than microlensing, or based on a possible trend inferred from some high-angular-resolution follow-up observation results for microlensing planets (Bhattacharya et al. 2021).

Koshimoto et al. (2021b) imposed constraints on the r value, $r = 0.2 \pm 0.4$. Because this is consistent with $r = 0$, the traditional assumption of $r = 0$ was observationally justified. On the other hand, the previous study has a large uncertainty

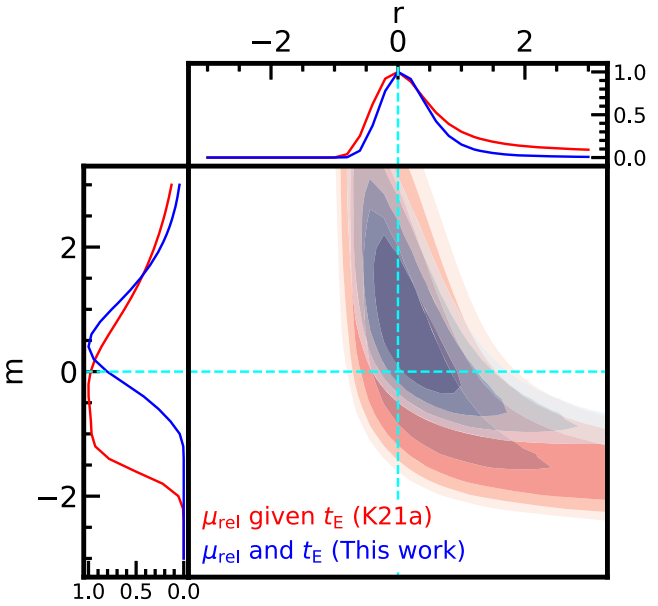

Figure 5. Comparison of the results obtained via the Koshimoto et al. (2021b) method (red) that uses one-dimensional $\mu_{\rm rel}$ distributions for given $t_{\rm E}$ and this study's method (blue) that uses two-dimensional ($t_{\rm E}$, $\mu_{\rm rel}$) distributions.

regarding the host star mass dependence. Our results succeeded in making more constraints, and in particular, found that $m > 0$ is preferred for microlensing planetary events with $q \gtrsim 10^{-3}$. Therefore, using $m > 0$ (e.g., $m = 1$) might be a better choice than the traditional assumption of $m = 0$ for events with $q \gtrsim 10^{-3}$.

4.3. Comparison with the Previous Method

As we discussed in Section 1, this study is an extension of Koshimoto et al. (2021b). As a comparison, we analyzed the same sample of 22 planets used in our study, but this time via the method of Koshimoto et al. (2021b). Figure 5 compares the result with these two methods. This corresponds to a comparison between the result using the one-dimensional distribution of $\mu_{\rm rel}$ for given $t_{\rm E}$ and the result using the two-dimensional distribution of $t_{\rm E}$ and $\mu_{\rm rel}$. As expected, Figure 5 shows that using a two-dimensional distribution allows for more constraint of m and r values compared to using the one-dimensional distribution.

A disadvantage of the new method is that the number of samples is limited to apply proper detection efficiency as described in Section 3.1. In fact, in this study, six planetary events from Gould et al. (2010) and Cassan et al. (2012) were excluded for that reason. On the other hand, the previous method has the advantage of easily increasing the sample size by avoiding the detection efficiency issue, and Koshimoto et al. (2021b) used the six events mentioned above in addition to the 22 events used in this study.

Nevertheless, we were able to impose a stronger constraint of $m = 0.50^{+0.90}_{-0.70}$, compared to the $m = 0.2 \pm 1.0$ of Koshimoto et al. (2021b). This fact indicates that the two-dimensional approach is more informative than the one-dimensional approach, even considering the decrease in the number of samples. Hence, when high detection efficiency is available, it is preferable to use the method described in this study as much as possible. Note that both methods require a Galactic model, and one needs to ensure that the model is unbiased, for instance, by a sanity test as performed in Appendix B.

5. Conclusion

We estimated the dependence of planet frequency on the host star mass and the Galactocentric distance by comparing the ($t_{\rm E}$, $\mu_{\rm rel}$) distribution of the 22 microlensing planetary events from S16 with the one expected from the Galactic model. By assuming the power law $P_{\rm host} \propto M_{\rm L}^{m} \times R_{\rm L}^{r}$ as the planet-hosting probability, we estimated $r = 0.10^{+0.51}_{-0.37}$ and $m = 0.50^{+0.90}_{-0.70}$. We also divided our sample into subsamples by the mass ratios and found that the giant planet sample with $q \gtrsim 10^{-3}$ prefers $m > 0$ whereas m is consistent with 0 for the lower-mass ratio samples. This suggests that massive planets are more likely to exist around more massive stars. On the other hand, there is no significant preference in either positive or negative r, i.e., no large dependence of planet frequency on the Galactocentric distance, which is consistent with the result of Koshimoto et al. (2021b).

The analysis method of this study and Koshimoto et al. (2021b) can be used for planet samples from other microlensing survey projects. The Korea Microlensing Telescope Network (KMTNet; Kim et al. 2016) has operated their microlensing survey since 2016, and more than 200 planets have already been detected. The PRime-focus Infrared Microlensing Experiment (PRIME) began their survey toward the Galactic bulge and center in 2023 (Kondo et al. 2023; Yama et al. 2023). PRIME is expected to discover 42–50 planets per year (Kondo et al. 2023). The Nancy Grace Roman Space Telescope is planned to launch in late 2026 (Spergel et al. 2015) and a total of ∼1400 planets are expected to be discovered (Penny et al. 2019). A similar analysis with the planet sample by these surveys can further constrain the dependence of planet frequency on the host star mass and the location in our Galaxy.

Acknowledgments

K.N. acknowledges support from a Scholarly Studies grant from the Smithsonian Institution and was supported by the Scholarship of the Graduate School of Science of "Osaka University Foundation for the Future" for overseas research activities in 2023, JSPS Core-to-Core Program (grant No.: JPJSCCA20210003), and the Ono Scholarship Foundation for the public interest incorporated foundation. D.S. was supported by JSPS KAKENHI grant No. JP19KK082. We are grateful to Kento Masuda and Ryusei Hamada for their insightful discussions.

Appendix A
Validation of Method by Mock Data Analysis

As described in Section 2, we conduct mock data simulations to validate our method. We adopt a certain (m,r) value and generate 50 mock planetary event samples with weights of $\Gamma_{\rm host}(t_{\rm E}, \mu_{\rm rel}|m, r) \times \epsilon$. This sample can be regarded as a sample of actually observed planetary events in the virtual galaxy that has a specific value of (m,r) and we know this specific value. Therefore, if the analysis method is correct, it is expected that we can reproduce the actual values of (m,r) by analyzing these mock planetary events. We produced mock data with nine combinations of $m = -1, 0, 1$, and $r = -1, 0, 1$, and analyzed these artificial planetary events.

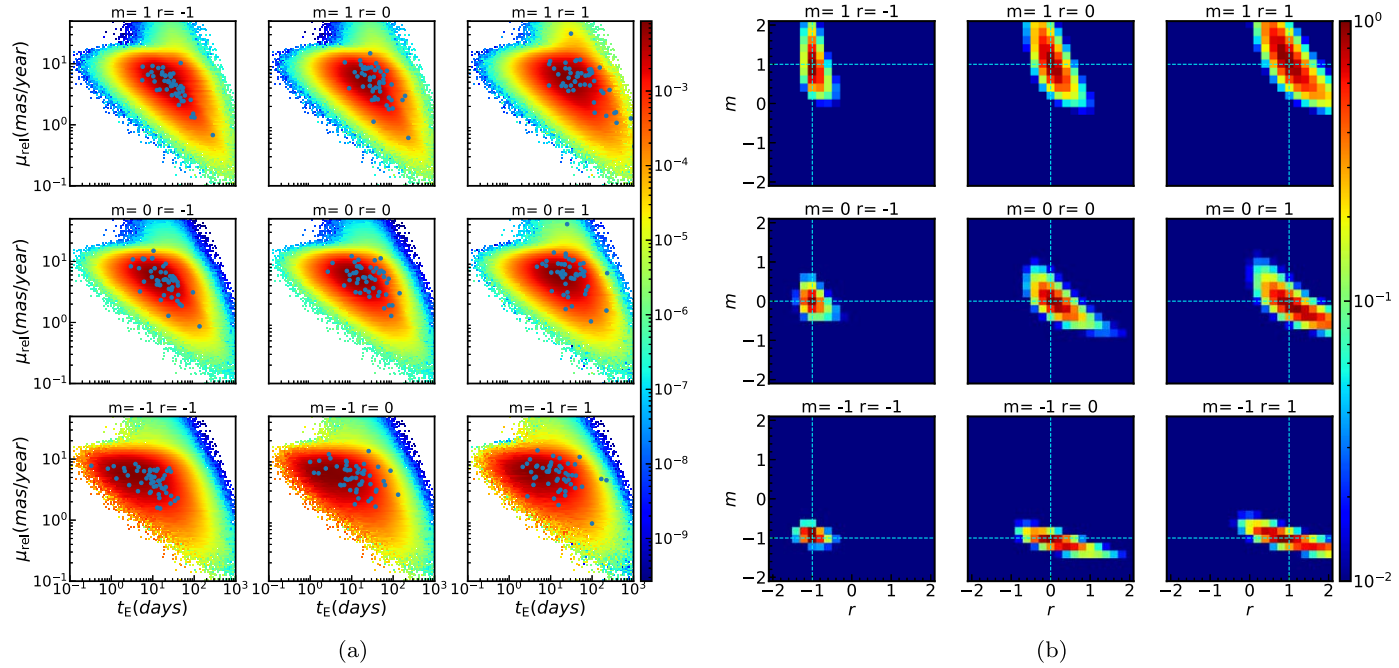

Figure 6. (a) Two-dimensional distribution of t_E and μ_{rel}. The blue dots show the 50 samples used in this mock data analysis. (b) Result of the mock data analysis. Each panel has a different correct (m,r) value, and the intersection of the dotted lines shows its correct value. Each analysis is based on 50 artificially generated samples, weighted according to their respective (m,r) values.

Figure 6(a) shows the distribution of t_E and μ_{rel} under each (m, r) value, and Figure 6(b) shows the result of the likelihood analysis for the mock data indicated by dots in Figure 6(a). It can be seen that the correct m and r values are well reproduced in each analysis regardless of the true (m, r) values, although the strength of the (m,r) correlation differs depending on the true (m,r) values.

Appendix B
Verification of Galactic Model by MOA-II FSPL Sample

Although our method was validated by the mock data analysis in Appendix A, the simulations using mock data are not sufficient to truly justify the results from this study, because the same Galactic model was used both to generate the mock data and to calculate the likelihood. Since the real data are generated following the real distribution of our Galaxy, the validity of the Galactic model needs to be verified.

In this section, we compare the (t_E, μ_{rel}) distribution predicted by the Galactic model with the distribution of the finite-source point-lens (FSPL) event sample from the MOA-II 9 yr Galactic bulge survey (K23) to evaluate the amount of bias in the Galactic model that would affect our measurement of (m, r). Because the FSPL sample should reflect the distribution of random stars in our Galaxy, their (t_E, μ_{rel}) distribution can be fairly compared with the predicted distribution by the Galactic model if the detection efficiency is properly taken into account.

For the comparison in this section, we use a slightly modified version of Equation (4) for the model-predicted distribution, i.e.,

$$f_{\rm FSPL}(t_{\rm E}^{\rm (obs)}, \mu_{\rm rel}^{\rm (obs)}|m_{\rm bias}, r_{\rm bias}) = \int dt_{\dot{\rm E}} d\mu_{\rm rel} [k(t_{\rm E}^{\rm (obs)}, \mu_{\rm rel}^{\rm (obs)}; t_{\dot{\rm E}}, \mu_{\rm rel}) \Gamma_{\rm bias}(t_{\dot{\rm E}}, \mu_{\rm rel}|m_{\rm bias}, r_{\rm bias}) \epsilon_{\rm FSPL}(t_{\dot{\rm E}}, \mu_{\rm rel})],$$

where $(t_{\rm E}^{\rm (obs)}, \mu_{\rm rel}^{\rm (obs)})$ are from the MOA-II 9 yr FSPL sample described in Section B.1, and $\epsilon_{\rm FSPL}(t_{\rm E}, \mu_{\rm rel})$ is the detection efficiency corresponding to the sample described in Section B.2. $\Gamma_{\rm bias}(t_{\rm E}, \mu_{\rm rel}|m_{\rm bias}, r_{\rm bias})$ is defined as

$$\Gamma_{\rm bias}(t_{\rm E}, \mu_{\rm rel}|m_{\rm bias}, r_{\rm bias}) \propto \int dM_{\rm L} dR_{\rm L} \Gamma_{\rm FSPL}(t_{\rm E}, \mu_{\rm rel}, M_{\rm L}, R_{\rm L}) M_{\rm L}^{m_{\rm bias}} R_{\rm L}^{r_{\rm bias}},$$

where $\Gamma_{\rm FSPL}$ is the event rate for FSPL events calculated by the Galactic model and $\Gamma_{\rm FSPL} \propto \Gamma_{\rm all}\, \theta_{\rm E}^{-1}$. $m_{\rm bias}$ and $r_{\rm bias}$ are the parameters to quantify the bias level in the Galactic model, and $(m_{\rm bias}, r_{\rm bias}) = (0, 0)$ corresponds to no bias. We evaluate $(m_{\rm bias}, r_{\rm bias})$ for the Koshimoto et al. (2021a) Galactic model in Section B.3.

B.1. MOA-II 9 yr FSPL Sample

K23 systematically analyzed the MOA-II Galactic bulge survey data during the 9 yr from 2006 to 2014 and selected ∼3500 single-lens events. There are 13 FSPL events in the MOA-II 9 yr sample where the finite-source effect (Alcock et al. 1997; Yoo et al. 2004) was detected, and both t_E and μ_{rel} were measured thanks to the effect. Two of the FSPL events are free-floating planet candidates with $t_E < 0.5$ day, and modeling their distribution requires an additional part of the mass function for a planetary mass range that is irrelevant to our sample of the S16 events with $t_E > 2$ days. Therefore, we do not use those two events, and instead consider only the remaining 11 FSPL events. This corresponds to applying an additional selection criterion of $\theta_E > 0.03$ mas to the 9 yr sample in addition to the original selection criteria applied by K23. This additional selection criterion allows us to avoid considering events with extremely small θ_E and to erase the μ_{rel} dependency from the detection efficiency for single-lens events, $\epsilon_{SL}(t_E)$, which is defined below in Section B.2.

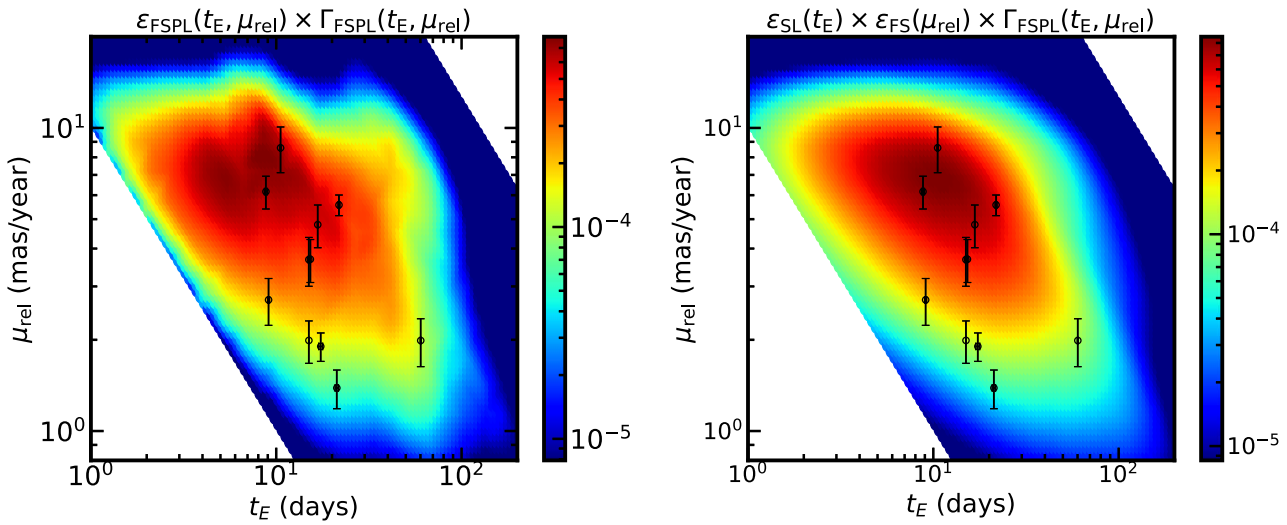

Figure 7. Comparison of the ($t_{\rm E}$, $\mu_{\rm rel}$) distributions for the MOA-II 9 yr FSPL sample between the observations (black points) and the prediction by the Galactic model combined with the detection efficiency (color maps) when ($m_{\rm bias}$, $r_{\rm bias}$) = (0, 0). The left panel calculates the detection efficiency, $\epsilon_{\rm FSPL}(t_{\rm E}, \mu_{\rm rel})$, without the separable assumption (Equation (B1)), whereas the right panel calculates the one with the separable assumption (Equation (B2)).

The black dots in the left panel of Figure 7 show the ($t_{\rm E}$, $\mu_{\rm rel}$) distribution of the selected 11 FSPL events.

B.2. Detection Efficiency

K23 performed image-level simulations of 6.4×10^7 artificial events to calculate the detection efficiency as a function of ($t_{\rm E}$, $\theta_{\rm E}$), which is equivalent to the detection efficiency as a function of ($t_{\rm E}$, $\mu_{\rm rel}$) because $\theta_{\rm E} = \mu_{\rm rel}\, t_{\rm E}$. However, their original detection efficiency is for their sample of ∼3500 single-lens events including both PSPL and FSPL events, and this is not suitable for our sample of the 11 FSPL events. Therefore, we recalculate the detection efficiency for our sample, $\epsilon_{\rm FSPL}(t_{\rm E}, \mu_{\rm rel})$, using their simulation results, via the following procedure.

Their simulated artificial events were distributed uniformly in $0 < u_0 < 1.5$, where u_0 is the impact parameter in units of $\theta_{\rm E}$. To define the detection efficiency against FSPL events that follow $\Gamma_{\rm FSPL} \propto \Gamma_{\rm all}\, \theta_{\rm E}^{-1}$, we first limit the artificial events to those with $0 < z_0 < 5$, where $z_0 \equiv u_0/\rho$ and $\rho = \theta_*/\theta_{\rm E}$ is the size of the angular source radius θ_* in units of $\theta_{\rm E}$. Then, we further limit the artificial events to those with $\theta_{\rm E} > 0.03$ mas as described in Section B.1. The remaining artificial events are used as the total number of valid simulated events, $N_{{\rm sim},z_0}$. Note that event counts here are done after considering the weight for each event based on its event rate given by Equation (13) of K23.

The next step is to count the number of events that pass the selection criteria for the FSPL events. There are two requirements to be selected as an FSPL event in K23: the first is to pass the selection criteria listed in Table 2 of K23 and be selected as a single-lens event, and the second one is to have a significant $\Delta\chi^2$ value between the best-fit PSPL and FSPL models (see Section 8 of K23 for the detail). We apply the same two-step criteria and count the number of events that pass the first step as $N_{\rm det,\ SL}$ and the ones that also pass the second step as $N_{\rm det,\ FSPL}$.

Ideally, the desired detection efficiency $\epsilon_{\rm FSPL}(t_{\rm E}, \mu_{\rm rel})$ can be simply calculated by

$$\epsilon_{\rm FSPL}(t_{\rm E}, \mu_{\rm rel}) = \frac{N_{\rm det,\ FSPL}(t_{\rm E}, \mu_{\rm rel})}{N_{{\rm sim},z_0}(t_{\rm E}, \mu_{\rm rel})}, \tag{B1}$$

where $N_{\rm det,\ FSPL}(t_{\rm E}, \mu_{\rm rel})$ and $N_{{\rm sim},z_0}(t_{\rm E}, \mu_{\rm rel})$ are subsamples of $N_{\rm det,\ FSPL}$ and $N_{{\rm sim},z_0}$ in a grid of ($t_{\rm E}$, $\mu_{\rm rel}$), respectively. However, the number of $N_{\rm det,\ FSPL}$ in each grid of ($t_{\rm E}$, $\mu_{\rm rel}$) is too small to have a precise value of $\epsilon_{\rm FSPL}(t_{\rm E}, \mu_{\rm rel})$, because the K23 simulation was not optimized for FSPL events. Therefore, we assume that $\epsilon_{\rm FSPL}(t_{\rm E}, \mu_{\rm rel})$ is separable as a product of two single variable functions, i.e.,

$$\epsilon_{\rm FSPL}(t_{\rm E}, \mu_{\rm rel}) \simeq \epsilon_{\rm SL}(t_{\rm E})\, \epsilon_{\rm FS}(\mu_{\rm rel}), \tag{B2}$$

where

$$\epsilon_{\rm SL}(t_{\rm E}) = \frac{N_{\rm det,\ SL}(t_{\rm E})}{N_{{\rm sim},z_0}(t_{\rm E})}, \tag{B3}$$

and

$$\epsilon_{\rm FS}(\mu_{\rm rel}) = \frac{N_{\rm det,\ FSPL}(\mu_{\rm rel})}{N_{\rm det,\ SL}(\mu_{\rm rel})}. \tag{B4}$$

Equation (B2) gives us a more precise $\epsilon_{\rm FSPL}(t_{\rm E}, \mu_{\rm rel})$ distribution than Equation (B1) because it enables us to use the numbers of $N_{\rm det,\ FSPL}$ distributed in one-dimensional bins of $\mu_{\rm rel}$ instead of the numbers distributed in two-dimensional grids of ($t_{\rm E}$, $\mu_{\rm rel}$).

The separable assumption of $\epsilon_{\rm FSPL}(t_{\rm E}, \mu_{\rm rel}) = \epsilon_{\rm SL}(t_{\rm E})\, \epsilon_{\rm FS}(\mu_{\rm rel})$ is reasonable because the detection efficiency for single-lens events, $\epsilon_{\rm SL}$, only depends on $t_{\rm E}$ for events with $\theta_{\rm E} > 0.03$ mas as shown in Figure 7 of K23. Also, the detection efficiency for the finite-source effect depends on the number of data points taken during the source radius crossing time, $t_* = \theta_*/\mu_{\rm rel}$. Because the angular source radius θ_* is independent of $t_{\rm E}$, the detection efficiency for the finite-source effect only depends on $\mu_{\rm rel}$.

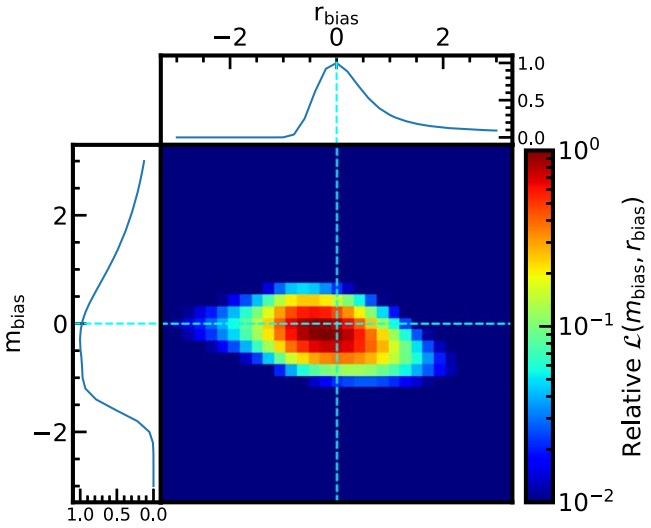

Figure 8. Relative likelihood distribution of ($m_{\rm bias}$, $r_{\rm bias}$) calculated by Equation (B5) for the Galactic model by Koshimoto et al. (2021a) when compared with the MOA-II 9 yr FSPL sample. The top panel shows a relative probability distribution of $r_{\rm bias}$ integrated uniformly over $-3 < m_{\rm bias} < 3$, and the side panel shows a relative probability distribution of $m_{\rm bias}$ integrated uniformly over $-3 < r_{\rm bias} < 3$.

The color maps in Figure 7 show the model-predicted ($t_{\rm E}$, $\mu_{\rm rel}$) distributions, i.e., $\Gamma_{\rm FSPL}(t_{\rm E}, \mu_{\rm rel}) \times \epsilon_{\rm FSPL}(t_{\rm E}, \mu_{\rm rel})$, where the left panel shows the one with $\epsilon_{\rm FSPL}(t_{\rm E}, \mu_{\rm rel})$ calculated using Equation (B1) and the right panel shows the one with $\epsilon_{\rm FSPL}(t_{\rm E}, \mu_{\rm rel})$ calculated using Equation (B2). As expected, the right panel shows a much smoother distribution than the left panel. At the same time, the two distributions look like they represent a similar distribution, indicating that the separable assumption is valid, at least to a good approximation.

B.3. Sanity Test for the Galactic Model

Figure 7 shows the comparison of the observational ($t_{\rm E}$, $\mu_{\rm rel}$) distribution from the MOA-II 9 yr FSPL sample (black dots) with the one from the Galactic model with ($m_{\rm bias}$, $r_{\rm bias}$) = (0, 0) (color map). It shows a good agreement between the observations and the model, which implies that the Galactic model by Koshimoto et al. (2021a) is not significantly biased. To quantify this, we calculate the likelihood distribution of ($m_{\rm bias}$, $r_{\rm bias}$) given by

$$\mathcal{L}(m_{\rm bias}, r_{\rm bias}) = \prod_i f_{\rm FSPL}\left(t_{{\rm E},i}^{\rm (obs)}, \mu_{{\rm rel},i}^{\rm (obs)} | m_{\rm bias}, r_{\rm bias}\right), \quad \text{(B5)}$$

and the result is shown in Figure 8. Figure 8 shows that the likelihood is distributed around ($m_{\rm bias}$, $r_{\rm bias}$) = (0, 0). The best grid is at ($m_{\rm bias}$, $r_{\rm bias}$) = (-0.2, -0.2), and the likelihood at ($m_{\rm bias}$, $r_{\rm bias}$) = (0, 0) is 0.80 relative to the best grid value. The median and 1σ uncertainty values are $m_{\rm bias} = -0.27^{+0.33}_{-0.32}$ and $r_{\rm bias} = -0.32^{+0.65}_{-0.61}$.

The fact that the likelihood distribution is consistent with ($m_{\rm bias}$, $r_{\rm bias}$) = (0, 0) means that the Galactic model by Koshimoto et al. (2021a) would not cause a significant bias in our estimation on (m, r), and we can securely use the model in our analysis in Section 3. The same test can be used for any other Galactic models to test their validity.

ORCID iDs

Kansuke Nunota https://orcid.org/0009-0005-3414-455X
Naoki Koshimoto https://orcid.org/0000-0003-2302-9562
Daisuke Suzuki https://orcid.org/0000-0002-5843-9433
Takahiro Sumi https://orcid.org/0000-0002-4035-5012
David P. Bennett https://orcid.org/0000-0001-8043-8413
Yuki Hirao https://orcid.org/0000-0003-4776-8618
Sean K. Terry https://orcid.org/0000-0002-5029-3257

References

Alcock, C., Allen, W. H., Allsman, R. A., et al. 1997, ApJ, 491, 436
Beaulieu, J.-P., Bennett, D. P., Batista, V., et al. 2016, ApJ, 824, 83
Bennett, D. P., Batista, V., Bond, I. A., et al. 2014, ApJ, 785, 155
Bennett, D. P., Bond, I. A., Udalski, A., et al. 2008, ApJ, 684, 663
Bennett, D. P., Rhie, S. H., Nikolaev, S., et al. 2010, ApJ, 713, 837
Bhattacharya, A., Bennett, D. P., Beaulieu, J. P., et al. 2021, AJ, 162, 60
Blackman, J. W., Beaulieu, J. P., Bennett, D. P., et al. 2021, Natur, 598, 272
Burn, R., Schlecker, M., Mordasini, C., et al. 2021, A&A, 656, A72
Cassan, A., Kubas, D., Beaulieu, J.-P., et al. 2012, Natur, 481, 167
Clarke, J. P., Wegg, C., Gerhard, O., et al. 2019, MNRAS, 489, 3519
Fulton, B. J., Rosenthal, L. J., Hirsch, L. A., et al. 2021, ApJS, 255, 14
Gaia Collaboration, Katz, D., Antoja, T., et al. 2018, A&A, 616, A11
Gaudi, B. S., Bennett, D. P., Udalski, A., et al. 2008, Sci, 319, 927
Gould, A., Dong, S., Gaudi, B. S., et al. 2010, ApJ, 720, 1073
Ida, S., & Lin, D. N. C. 2005, ApJ, 626, 1045
Ishitani Silva, S., Ranc, C., Bennett, D. P., et al. 2022, AJ, 164, 118
Johnson, J. A., Aller, K. M., Howard, A. W., et al. 2010, PASP, 122, 905
Johnson, J. A., Butler, R. P., Marcy, G. W., et al. 2007, ApJ, 670, 833
Kim, S.-L., Lee, C.-U., Park, B.-G., et al. 2016, JKAS, 49, 37
Kondo, I., Sumi, T., Koshimoto, N., et al. 2023, AJ, 165, 254
Koshimoto, N., Baba, J., & Bennett, D. P. 2021a, ApJ, 917, 78
Koshimoto, N., Bennett, D. P., Suzuki, D., et al. 2021b, ApJL, 918, L8
Koshimoto, N., & Ranc, C. 2022, nkoshimoto/genulens: Release version 1.2, Zenodo, doi:10.5281/zenodo.4784948
Koshimoto, N., Shvartzvald, Y., Bennett, D. P., et al. 2017, AJ, 154, 3
Koshimoto, N., Sumi, T., Bennett, D. P., et al. 2023, AJ, 166, 107
Kunder, A., Koch, A., Rich, R. M., et al. 2012, AJ, 143, 57
Liu, B., Lambrechts, M., Johansen, A., et al. 2019, A&A, 632, A7
Liu, B., Lambrechts, M., Johansen, A., et al. 2020, A&A, 638, A88
Mróz, P., Udalski, A., Skowron, J., et al. 2017, Natur, 548, 183
Mróz, P., Udalski, A., Skowron, J., et al. 2019, ApJS, 244, 29
Mulders, G. D. 2018, Handbook of Exoplanets (Berlin: Springer), 153
Nataf, D. M., Gould, A., Fouqué, P., et al. 2013, ApJ, 769, 88
Olmschenk, G., Bennett, D. P., Bond, I. A., et al. 2023, AJ, 165, 175
Penny, M. T., Gaudi, B. S., Kerins, E., et al. 2019, ApJS, 241, 3
Reffert, S., Bergmann, C., Quirrenbach, A., et al. 2015, A&A, 574, A116
Rich, R. M., Reitzel, D. B., Howard, C. D., et al. 2007, ApJL, 658, L29
Rosenthal, L. J., Fulton, B. J., Hirsch, L. A., et al. 2021, ApJS, 255, 8
Shin, I.-G., Yee, J. C., Zang, W., et al. 2023, AJ, 166, 104
Shvartzvald, Y., Maoz, D., Kaspi, S., et al. 2014, MNRAS, 439, 604
Smith, L. C., Lucas, P. W., Kurtev, R., et al. 2018, MNRAS, 474, 1826
Spergel, D., Gehrels, N., Baltay, C., et al. 2015, arXiv:1503.03757
Suzuki, D., Bennett, D. P., Sumi, T., et al. 2016, ApJ, 833, 145
Terry, S. K., Bennett, D. P., Bhattacharya, A., et al. 2022, AJ, 164, 217
Yama, H., Suzuki, D., Miyazaki, S., et al. 2023, JAI, 12, 2350004
Yee, J. C., Shvartzvald, Y., Gal-Yam, A., et al. 2012, ApJ, 755, 102
Yoo, J., DePoy, D. L., Gal-Yam, A., et al. 2004, ApJ, 603, 139
Zhu, W., Penny, M., Mao, S., et al. 2014, ApJ, 788, 73